The Astrophysical Journal, 996:60 (13pp), 2026 January 1 https://doi.org/10.3847/1538-4357/ae1fd6

IGR J17091−3624: Newly Formed Periodic Dips and Multiwavelength Activity during the 2025 Outburst

Zikun Lin[1,2], Yanan Wang[1], Shuyuan Wei[3], Yongkang Sun[1,3], Long Ji[4], Samaporn Tinyanont[5], Meng Sun[1,6], Song Wang[1,7], Diego Altamirano[8], Douglas J. K. Buisson[9], Wenxiong Li[1], Qian Chen[1], Jifeng Liu[1,3,7,10], Shuang-Nan Zhang[3,11], Wei Wang[1], Zhen Guo[12,13], Pathompong Butpan[5], and Rungrit Anutarawiramkul[5]

[1] National Astronomical Observatories, Chinese Academy of Sciences, Beijing 100101, People's Republic of China; wangyn@bao.ac.cn
[2] Department of Astronomy, Xiamen University, Xiamen, Fujian 361005, People's Republic of China
[3] School of Astronomy and Space Sciences, University of Chinese Academy of Sciences, Beijing 100049, People's Republic of China
[4] School of Physics and Astronomy, Sun Yat-sen University, Zhuhai 519082, People's Republic of China
[5] National Astronomical Research Institute of Thailand (Public Organisation), 260 Moo 4, T. Donkaew, A. Maerim, Chiangmai 50180, Thailand
[6] Center for Interdisciplinary Exploration and Research in Astrophysics (CIERA), 1800 Sherman, Evanston, IL 60201, USA
[7] Institute for Frontiers in Astronomy and Astrophysics, Beijing Normal University, Beijing 102206, People's Republic of China
[8] School of Physics and Astronomy, University of Southampton, Southampton, Hampshire SO17 1BJ, UK
[9] Independent
[10] New Cornerstone Science Laboratory, National Astronomical Observatories, Chinese Academy of Sciences, Beijing 100012, People's Republic of China
[11] Key Laboratory of Particle Astrophysics, Institute of High Energy Physics, Chinese Academy of Sciences, 19B Yuquan Road, Beijing 100049, People's Republic of China
[12] Instituto de Física y Astronomía, Universidad de Valparaíso, ave. Gran Bretaña, 1111, Casilla 5030, Valparaíso, Chile
[13] Millennium Institute of Astrophysics, Nuncio Monseñor Sotero Sanz 100, Of. 104, Providencia, Santiago, Chile

Received 2025 August 30; revised 2025 November 11; accepted 2025 November 12; published 2025 December 24

Abstract

The black hole low-mass X-ray binary (LMXB) candidate IGR J17091–3624 experienced a hard-state-only outburst in 2025. In this paper, we show that IXPE detected a series of intermittent X-ray dips, spanning a total interval of ~1 day. Subsequent observations with NICER, the Einstein Probe, NuSTAR, and Swift reveal that these dips recur with a period of 2.83 ± 0.07 days and are accompanied by an increase in spectral hardness. This is the first time such quasiperiodic dipping behavior has been observed in this target since discovery. Our spectral analysis shows that the dips can be explained by obscuration from an ionized absorber characterized by an ionization parameter of $\log \xi \sim 1\text{–}3\ \mathrm{erg\,cm\,s^{-1}}$ and an equivalent hydrogen column density of $N_{\mathrm{H}}^{\mathrm{zxipcf}} \sim (1-30) \times 10^{22}\ \mathrm{cm^{-2}}$. The periodic reappearance of the absorber is likely caused by obscuring material located in the outer accretion disk, modulated by the binary orbital period. If confirmed, this period would suggest that the donor star in IGR J17091–3624 has deviated from the standard main-sequence evolutionary path and is likely a (partially) stripped giant. In the optical band, no significant periodicity or correlation with the X-ray dips was detected, whereas the radio counterpart exhibited a flat to steep spectrum, in contrast to the inverted spectrum typically observed during the hard state of LMXBs.

Unified Astronomy Thesaurus concepts: Black hole physics (159); Accretion (14); X-ray transient sources (1852)

1. Introduction

Low-mass X-ray binaries (LMXBs) are celestial systems consisting of a neutron star or black hole in a close orbit, accreting material via Roche-lobe overflow from a donor star. Periodic X-ray dips and/or eclipses, occurring on timescales of hours to days, have been observed in approximately 30 Galactic LMXBs (A. Avakyan et al. 2023), and are widely regarded as reliable indicators of high inclination. Eclipses occur when the X-ray-emitting region is occulted by the companion star, leading to a near-total drop in X-ray intensity. In contrast, dips are typically less regular in periodicity, exhibit shallower decreases in X-ray intensity with variable profiles, and are associated with systems viewed at moderately high inclinations (60°–75°; J. Frank et al. 1987).

In LXMBs, dips are typically accompanied by spectral variations, often showing increased hardness ratios (HRs; see, e.g., N. E. White & J. H. Swank 1982; L. Boirin et al. 2005; M. Díaz Trigo et al. 2006; M. Shidatsu et al. 2013; D. J. K. Buisson et al. 2021). Accordingly, dipping phenomena are thought to result from the temporary obscuration of the central X-ray source by clumps of low-ionization material along the line of sight (see, e.g., L. Boirin et al. 2005; M. Díaz Trigo et al. 2006; M. Shidatsu et al. 2013). Furthermore, the relatively long recurrence timescales of these dips are generally consistent with the binary orbital period, suggesting that the obscuring material is located in the outer regions of the accretion disk and is likely associated with the mass transfer stream from the donor star (e.g., J. Frank et al. 1987; P. J. Armitage & M. Livio 1996, 1998). Among dipping LMXBs, some sources (such as EXO 0748–676 (D. Crampton et al. 1986) and MAXI J1659–152 (J. M. Corral-Santana et al. 2018)) also exhibit optical modulation at the same period as the X-ray dips, further supporting their orbital origin. In addition, dips can show evolving profiles and may even appear early in the outburst before disappearing later (e.g., E. Kuulkers et al. 2013; J. J. E. Kajava et al. 2019). This behavior can be qualitatively explained by disk precession (M. Díaz Trigo et al. 2009) or changes in the structure of the accretion disk (E. Kuulkers et al. 2013). Therefore, X-ray dips serve as powerful diagnostics, offering valuable insights into the orbital parameters and dynamics of X-ray binaries (XRBs), as well as the structure and behavior of their accretion disks.

IGR J17091–3624 is a Galactic low-mass black hole XRB (BHXRB) candidate, first discovered by INTEGRAL/IBIS in 2003 April (E. Kuulkers et al. 2003). Since then, it has undergone four additional outbursts in 2007, 2011, 2016, and 2022 (F. Capitanio et al. 2009; D. Altamirano et al. 2011; H. A. Krimm et al. 2011; J. M. Miller et al. 2016, 2022; J. Wang et al. 2024). Compared to other systems, IGR J17091–3624 displays a much richer variety of X-ray variability on timescales ranging from subseconds to minutes (D. Altamirano et al. 2011; J. M. C. Court et al. 2017; J. Wang et al. 2024), including heartbeat variability and quasiperiodic oscillations. However, system parameters, such as the black hole mass, orbital period, and the spectral type of the donor star, remain uncertain, hindering a deeper understanding of the origin of these variations.

In 2025 February, IGR J17091–3624 underwent a new outburst (J. Rodriguez et al. 2025; F. Vincentelli et al. 2025), which coincided with an optical rebrightening (K. Fialova et al. 2025; P. Saikia et al. 2025). Follow-up observations were triggered with several X-ray telescopes. Among them, Imaging X-ray Polarimetry Explorer (IXPE; M. C. Weisskopf et al. 2022) conducted a long observation of IGR J17091–3624 from 2025 March 7 to 10, during which dips were detected only on approximately one day of the exposure (M. Ewing et al. 2025). The overlapped Nuclear Spectroscopic Telescope Array (NuSTAR; F. A. Harrison et al. 2013) observation confirms the presence of dips (M. Ewing et al. 2025). Subsequent spectral analyses using NuSTAR observations have attributed these dips to absorption (O. K. Adegoke et al. 2025; D. Debnath et al. 2025). M. Pahari et al. (2013) had previously reported dips in IGR J17091–3624 during its 2011 outburst, though these were distinct from absorption dips. The appearance of absorption dips in IGR J17091–3624 in 2025 presents an opportunity to probe its binary system parameters. In this work, we present a follow-up study of the X-ray dipping phenomenon in IGR J17091–3624, examine its multiwavelength emission, and discuss the properties and possible origins of these features.

2. Observations and Data Reduction

2.1. X-Ray Observations

This paper used X-ray data from Neutron Star Interior Composition ExploreR (NICER; K. C. Gendreau et al. 2016), Einstein Probe (EP) Follow-up X-ray Telescope (FXT; W. Yuan et al. 2022), the X-Ray Telescope (XRT) on board the Neil Gehrels Swift Observatory (Swift; D. N. Burrows et al. 2005), NuSTAR, and IXPE. Unless explicitly mentioned, the source region used to extract the X-ray data is centered at R.A. = $257\overset{\circ}{.}2817$ and decl. = (J2000). EP/FXT and Swift/XRT are hereafter referred to as EP and Swift, respectively, throughout this paper.

All X-ray spectra were rebinned using the `ftgrouppha` task (J. S. Kaastra & J. A. M. Bleeker 2016) from the FTOOLS package (J. K. Blackburn 1995), with the `optmin` option to ensure a minimum of 3 counts per bin. Spectral fitting was carried out in XSPEC v12.13.1 (K. A. Arnaud 1996) using C-statistics (W. Cash 1979; J. S. Kaastra 2017), the abundance tables and photoelectric cross sections were taken from J. Wilms et al. (2000) and D. A. Verner et al. (1996), respectively. Unless explicitly mentioned, the uncertainties for each fitting parameter in this work were calculated at the 1σ confidence level.

2.1.1. NICER

NICER monitored IGR J17091–3624 from 2025 March 15 to May 31 (PIs: F. Vincentelli, Z. Lin, G. Mastroserio, and F. Sanzenbacher). Raw data were downloaded from the High Energy Astrophysics Science Archive Research Center (HEASARC). Data processing and screening were performed with the `nicerl2` pipeline within HEASOFT v6.32.1 (HEASARC 2014), applying the calibration files in version xti20221001. The light curves and spectra were generated with `nicerl3-lc` and `nicerl3-spect`, respectively. To minimize the impact of background flares and ensure an adequate signal-to-noise ratio (SNR), we regenerated the good time intervals (GTIs) by selecting periods with a 12–15 keV count rate below 0.5 counts s^{-1} and a minimum duration of 100 s. The spectrum background was estimated by the SCORPEON[14] background model. We let the `swcx` parameters free to vary to account for the excesses below 0.6 keV caused by the solar wind charge exchange. Spectral fitting was performed in the 0.5–15 keV energy range to characterize the background spectrum.

2.1.2. Einstein Probe

EP monitored IGR J17091–3624 from 2025 March 15 to May 31 (PI: Y. Wang). The raw data were processed using the FXT Data Analysis Software v1.10 with CALDB v1.10. Source light curve and spectra files for the two coaligned instruments, FXTA and FXTB, were generated following the standard procedure provided by the FXT Data Center.[15] The source was extracted using a circular region with a radius of 60″. The background region was selected using an annulus centered on the same coordinates as the source region, with inner and outer radii of 120″ and 240″, respectively.

2.1.3. Swift

Swift monitored IGR J17091–3624 from 2025 February 13 to June 28 (PI: S. Motta, M. Parra, and Y. Wang). The Swift light curves and spectrum were generated by the online tools at the UK Swift Science Data Centre[16] (P. A. Evans et al. 2007, 2009). The observation was split into snapshots (spacecraft orbits). Observations with fewer than 100 total counts were excluded to ensure a sufficient SNR for reliable spectral fitting.

2.1.4. IXPE

IXPE observed IGR J17091–3624 from 2025 March 7 to March 10 (PI: M. Parra). We downloaded the Level-2 event files from the HEASARC and applied barycenter corrections using the `barycorr` task from the FTOOLS package (J. K. Blackburn 1995). Source events were extracted using the `fselect` command from a circular region with a radius of 60″, while background events were selected from an annular

---

[14] https://heasarc.gsfc.nasa.gov/docs/nicer/analysis_threads/scorpeon-overview/

[15] http://epfxt.ihep.ac.cn/analysis

[16] https://www.swift.ac.uk/user_objects/

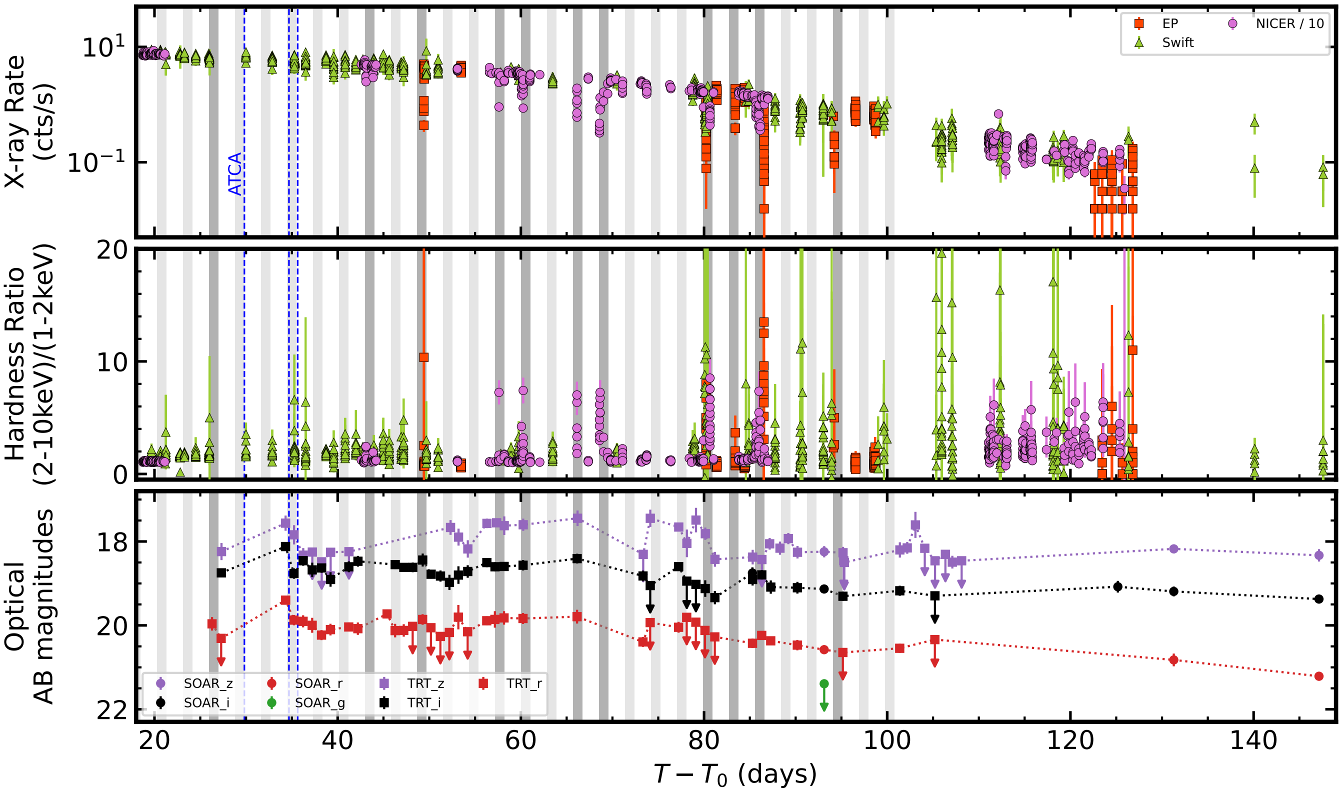

Figure 1. Top panel: X-ray light curves of IGR J17091–3624, observed by NICER (magenta), EP (red), and Swift (green). The NICER count rate was divided by 10 to align with those from the other telescopes. The light-gray shaded regions represent the predicted dipping episodes, while the darker gray regions represent the detected dipping episodes. The light curves were binned with a time resolution of 64 s. The blue vertical dashed lines indicate the epochs of the ATCA radio observations. Middle panel: HR derived from the above observations. Bottom panel: optical light curves of IGR J17091–3624 observed by SOAR and TRT in the g' (green), r' (red), i' (black), and z' (purple) filters. The downward arrows denote 3σ upper limits.

region with an inner radius of 120″ and an outer radius of 240″. We combined the light curves from the three detector units using *Stingray* (D. Huppenkothen et al. 2019).

2.1.5. NuSTAR

NuSTAR took five observations of IGR J17091 (PI: J. Garcia) between 2025 Feb 12 and March 9. The raw data were downloaded from HEASARC, and we conducted data processing using the NuSTAR Data Analysis Software version 1.9.7 with the Calibration Database version v20230420. The data were calibrated using the command *nupipeline*. We generated the source spectra and lightcurves for the two coaligned instruments, FPMA and FPMB, in the energy range 3–79 keV, respectively, along with their corresponding response and ancillary response files, using the *nuproducts* task. The extraction of the source region is circled with a radius of 100″, where the center is set at the emission peak. The background region was selected by placing a circular area with the same radius as the source region at the farthest corner of the image from the source center.

2.2. Optical Observations

Follow-up optical observations of IGR J17091–3624 were carried out by the Thai Robotic Telescope (TRT; Program ID: TRTC12A_003 and TRTC12B_003; PI: K. S. Tinyanont) and Southern Astrophysical Research telescope (SOAR; PI: I. El Mellah) from 2025 February 20 to June 30, using the g', r', i', and z' filters. The calibrated stars were selected within 60″of IGR J17091–3624 from SkyMapper Southern Survey Data Release 4 (C. A. Onken et al. 2024). Photometry was performed using the `photutils` package. The source aperture radius was chosen to enclose 90% of the photons, determined by averaging the widths from Gaussian profile fits in the vertical and horizontal directions.

There is an optical source located around 1″from IGR J17091–3624 (K. Fialova et al. 2025). Due to the limited spatial resolution of TRT and SOAR, the two sources could not be fully resolved in our observations. As a result, our photometry includes contributions from both IGR J17091–3624 and this nearby source. The observed magnitude during the 2025 outburst is at least one magnitude brighter than that measured when IGR J17091–3624 was in quiescence in 2024 by the Las Cumbres Observatory network of telescopes (K. Fialova et al. 2025). Additionally, SOAR can partially resolve the nearby source from IGR J17091–3624 (see Figure A1), and the difference image indicates that the rebrightening is primarily dominated by IGR J17091–3624 (see Appendix A for more details). We hence conclude that the optical variations observed in the bottom panel of Figure 1 are dominated by IGR J17091–3624.

2.3. Radio Observations

The Australia Telescope Compact Array (ATCA) observed IGR J17091–3624 during three epochs: 2025 February 23, February 28, and March 1 (Project: C3615; PI: Y. Wang). All observations were obtained in the 6D array configuration, which offers the longest baseline and hence the highest spatial resolution. Two spectral windows were centered at 5.5 GHz

Table 1
Radio Observations of IGR J17091–3624 by ATCA

MJD	Frequency (GHz)	Flux[a] (mJy)	Beam Size (Major) (arcsec)	Beam Size (Minor) (arcsec)	rms (mJy beam^{-1})	α
60729.8156	5.0	1.09 ± 0.03	13.15	1.52	0.022	−0.16 ± 0.02
	6.0	1.08 ± 0.03	11.37	1.26	0.019	...
	8.5	1.01 ± 0.03	8.10	0.93	0.018	...
	9.5	1.00 ± 0.03	6.99	0.80	0.017	...
60734.6821	5.0	1.01 ± 0.04	11.30	1.86	0.023	−0.51 ± 0.07
	6.0	0.90 ± 0.04	9.42	1.57	0.021	...
	8.5	0.80 ± 0.03	6.68	1.12	0.016	...
	9.5	0.71 ± 0.03	5.63	0.99	0.015	...
60735.6355	5.0	0.88 ± 0.08	9.64	1.76	0.044	−0.67 ± 0.04
	6.0	0.80 ± 0.08	8.16	1.48	0.040	...
	8.5	0.62 ± 0.06	5.93	1.07	0.027	...
	9.5	0.57 ± 0.07	4.88	0.93	0.025	...

Note.
[a] Integrated flux density.

and 9.0 GHz, each with a bandwidth of 2 GHz. Absolute flux density and bandpass calibration were performed using 1934–638 for the first epoch and 0823–500 for the subsequent two epochs, when 1934–638 was below the horizon. 1714–336 served as the phase calibrator throughout. No further ATCA observations were conducted after 2025 March, as the array entered the commissioning phase of the Broadband Integrated GPU Correlator for ATCA.

We reduced the data using the Common Astronomy Software Application (CASA v6.6.5, CASA Team et al. 2022). After standard calibration procedures, we imaged the calibrated visibilities using the CASA task `tclean` with Briggs weighting (robust = 0.5), and generated four 1 GHz-wide subband images centered at 5.0, 6.0, 8.5, and 9.5 GHz to characterize the spectral evolution of the source. Flux densities were extracted with the task `imfit`, fitting a single Gaussian component at the position of IGR J17091–3624. The quoted uncertainty is the quadrature sum of the statistical error returned by `imfit`, and a 5% systematic term accounts for the absolute flux-density scale. The resulting measurements for all epochs are listed in Table 1. The time of the ATCA observations is indicated by blue dashed lines in Figure 1.

3. Results

3.1. X-Ray Timing Analysis

Figure 1 shows the long-term light curves and HR from NICER, EP, and Swift observations. The HR is defined as the hard X-ray (2–10 keV) count rate divided by the soft X-ray (1–2 keV) count rate. In this study, we adopted MJD 60700 as the starting point (T_0) of the dataset. Approximately 27 days after T_0, a series of repeated dips were observed by IXPE, NICER, NuSTAR, EP, and Swift. During these dips, an increase in HR was observed, indicating that the flux reduction was more pronounced in the soft X-rays than in the hard X-rays.

Among these observations, NICER provided the most extensive coverage of the outburst, detecting seven prominent dip series (defined as NICER HR > 2) before day 100. After day 100, the X-ray emission exhibited a more rapid decline. Concurrently, the variability increased and became more irregular, accompanied by increased fluctuations in the HR. These fluctuations make it difficult to reliably identify dips in the light curve. Therefore, data collected after day 100 are excluded from the period determination.

To measure the periodicity of these dips, we first detrended the NICER soft X-ray light curve within the first 100 days by fitting a broken exponential decay model (A. R. King & H. Ritter 1998; T. Shahbaz et al. 1998):

$$f(x) = \begin{cases} N\exp\left(-\frac{x-x_{\rm b}}{\tau_1}\right), & \text{if } x \leqslant x_{\rm b} \\ N\exp\left(-\frac{x-x_{\rm b}}{\tau_2}\right), & \text{if } x \geqslant x_{\rm b} \end{cases}, \quad (1)$$

where $x_{\rm b}$ denotes the break time, τ_1 and τ_2 are the e-folding timescales before and after the break, respectively, and N is the normalization parameter. We note that this function is employed to detrend the long-term decay of the X-ray light curve; alternative forms, such as a broken linear function or a combination of exponential and linear components, can also describe the decay and do not substantially affect our subsequent analysis. The fit was performed using data with HR< 1.2, in order to minimize the influence of the dips. The light curve was binned at 16 s. We then applied the Lomb–Scargle periodogram (LSP) method, as implemented in the `astropy` library (Astropy Collaboration et al. 2022), to the detrended light curve to search for periodic signals. The LSP was logarithmically rebinned with a factor of 0.01. As a first approximation, we estimated the peak period and its uncertainty by fitting a Gaussian to the peak profile, yielding 2.83 ± 0.07 days (Figure 2).

To evaluate the significance of this detected periodicity, we first modeled the noise level in the LSP using a double broken power law to account for the white and red noise components:

$$f(x) = \begin{cases} N\left(\frac{x}{x_{\rm b1}}\right)^{p_1}, & \text{if } x \leqslant x_{\rm b1} \\ N\left(\frac{x}{x_{\rm b1}}\right)^{p_2}, & \text{if } x_{\rm b1} \leqslant x \leqslant x_{\rm b2}, \\ N\left(\frac{x_{\rm b2}}{x_{\rm b1}}\right)^{p_2}\left(\frac{x}{x_{\rm b2}}\right)^{p_3}, & \text{if } x \geqslant x_{\rm b2} \end{cases} \quad (2)$$

where $x_{\rm b1}$ and $x_{\rm b2}$ represent the two break frequencies, p_1, p_2, and p_3 denote the power-law index of the three spectral

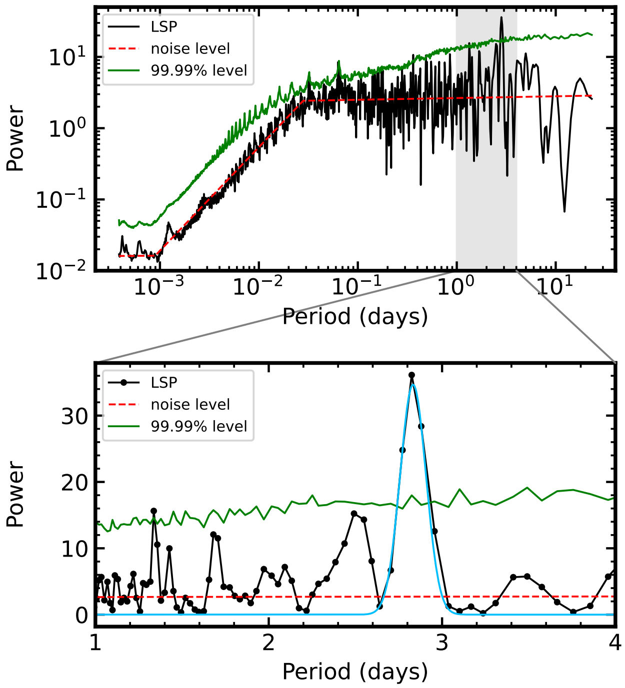

Figure 2. Top panel: LSP of the detrended NICER light curve. The red dashed line indicates the noise level, while the green line marks the 99.99% (4σ) confidence level. Bottom panel: zoomed-in view of the LSP around the most prominent peak. The blue curve shows the best-fitting Gaussian profile centered at 2.83 ± 0.07 days.

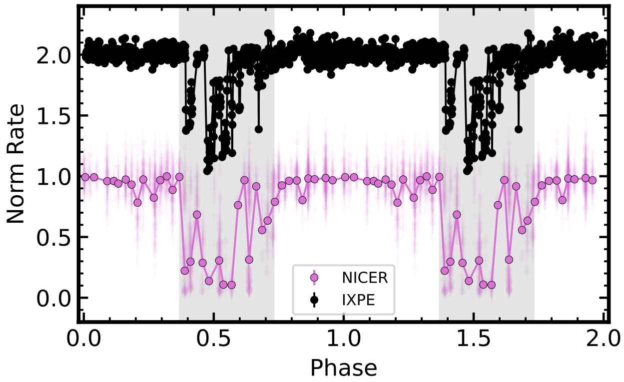

Figure 3. Folded soft X-ray light curve from NICER (detrended), shown alongside the IXPE light curve, using a period of 2.84 days. The NICER phase curve is rebinned into 0.025 phase units (corresponding to 0.07 days) using a weighted mean for clarity, with the original phase curve shown transparently. The gray shaded regions represent the dipping periods with a duration of 0.36 phase units (1 day).

segments, and N is the normalization parameter. Subsequently, we generated 50,000 simulated light curves using the DELightcurveSimulation[17] code (S. D. Connolly 2016), with the Emmanoulopoulos method (D. Emmanoulopoulos et al. 2013). Then, we generated the LSP of the simulated light curves and estimated their power distribution to determine the significance levels. The detected periodic signal exceeded a 99.99% (4σ) confidence level based on these simulations, robustly indicating that the period is real.

We folded the NICER light curves over the period uncertainty range of 2.83 ± 0.07 days, in steps of 0.01 days, and found that a period of 2.84 days provides the best phase alignment with the IXPE observations. The series of dips spans approximately 1 day, corresponding to a phase interval of 0.36 (see Figure 3). Under the assumption that the dips exhibit no phase shift over time, we adopted 2.84 days as the period for further analysis and used it to search for other potential dipping episodes.

Based on the above period, we identified eight dips in the EP, NuSTAR, and Swift data within the first 100 days of the outburst, four of which occurred outside NICER coverage. In total, 11 of the 29 predicted dipping episodes were detected; apart from the very first NICER observations (days 20.3–21.3), the remaining missed episodes were due to a lack of coverage. The identification of the nondetection in this NICER observation is based on the criterion that $\mathrm{HR} < 2$, and that spectral modeling does not statistically require an additional absorption component (see Section 3.2 for details), with ΔC-stat < 1 for two additional degrees of freedom (dof). This absence suggests that the dipping behavior may have developed gradually over the course of the outburst.

3.2. X-Ray Spectral Analysis

To investigate the origin of the dips, we conducted spectral analyses throughout the outburst. Initially, we modeled individual spectra on a GTI basis using an absorbed power-law model (`tbabs×powerlaw`). For the EP and NuSTAR observations, we jointly fitted their spectrum from the two coaligned units, using a `constant` parameter to account for calibration differences. This model provided a good fit to the continuum during the nondipping episodes, with the photon index (Γ) remaining below 2 within uncertainties. This suggests that IGR J17091–3624 has been in the hard state throughout the outburst. We also tested adding a disk blackbody component (`diskbb`; K. Mitsuda et al. 1984), but it did not result in significant improvement to the fit. Therefore, we applied the absorbed `powerlaw` model to describe the spectra from all detectors. The best-fitting parameters for each individual spectrum are shown in Figure 4.

As shown in Figure 4, the dipping episodes are accompanied by an increase in the column density ($N_{\mathrm{H}}^{\mathrm{tbabs}}$), indicating the presence of additional absorbing materials. Furthermore, we noticed a coupling between $N_{\mathrm{H}}^{\mathrm{tbabs}}$ and Γ, with the column density increasing as the photon index decreases. In several cases, a noticeable excess appears in the residuals around the 1–2 keV energy band, suggesting that neutral absorption alone is insufficient to fully explain the observed dips. After day 100, $N_{\mathrm{H}}^{\mathrm{tbabs}}$ gradually increased, suggesting an evolution of the absorbing material along the line of sight.

To account for the additional absorption component, we first included an ionized absorber component, `zxipcf`, resulting in a model: `constant×tbabs×zxipcf×powerlaw`. The `constant` component was used to account for calibration between different instruments. Moreover, to separate the ionized absorption from the continuum, we performed joint spectral fits of dipping and adjacent nondipping episodes within the same cycle (±1.4 days). The time coverage of each joint fit episode is shown by the orange shaded region in the right panel of Figure B1. Assuming the continuum and interstellar absorption do not vary within a cycle, we tied the `tbabs` and `powerlaw` parameters across dipping and

---

[17] https://github.com/samconnolly/DELightcurveSimulation

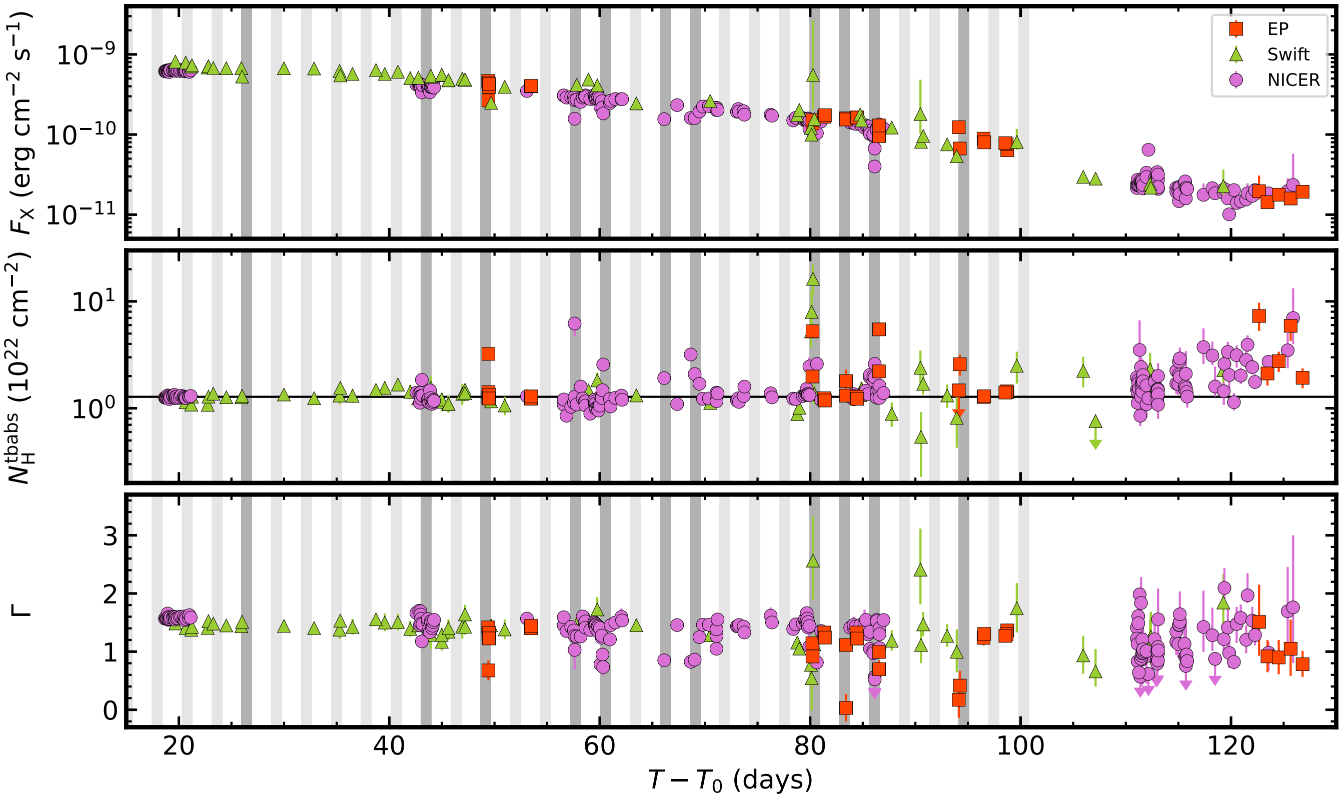

Figure 4. Evolution of spectral parameters derived from individual fitting, with the unabsorbed flux measured in the 0.5–10 keV band. Due to a different energy coverage, we do not include the IXPE and NuSTAR data in this plot. The colors are defined the same as in Figure 1. The horizontal black line in the middle panel indicates the median value of the $N_{\mathrm{H}}^{\mathrm{tbabs}}$ and is included to guide the eye for parameter evolution.

nondipping intervals. In addition, we observed a flux decrease of 3%–15% above 20 keV in the NuSTAR data during the dipping intervals. This hard absorption may arise from Compton scattering, modeled with the `cabs` component, which reduces the flux without altering the spectral shape by scattering photons out of the line of sight. Overall, we updated the model to `constant×tbabs×zxipcf×cabs×powerlaw`. Since freeing the covering fraction (f_{cov}) in the `zxipcf` component did not significantly improve the fit, we fixed it at 1 during dipping intervals and 0 during nondipping intervals to minimize parameter coupling. The equivalent hydrogen column density ($N_{\mathrm{H}}^{\mathrm{zxipcf}}$) and ionization parameter ($\log\xi$) were allowed to vary during the dipping intervals. Additionally, we set the equivalent hydrogen column density in the `cabs` component, $N_{\mathrm{H}}^{\mathrm{cabs}}$, to $1.21 \times N_{\mathrm{H}}^{\mathrm{zxipcf}}$ during the dipping intervals, and to zero during the nondipping intervals. The factor 1.21 is adopted from (B. Stelzer et al. 1999; M. Díaz Trigo et al. 2012) to account for the number of electrons per hydrogen atom in solar-abundance material. Overall, the free parameters include $N_{\mathrm{H}}^{\mathrm{tbabs}}$, $N_{\mathrm{H}}^{\mathrm{zxipcf}}$, $\log\xi$, Γ, and the normalization of the `powerlaw` component. We show three examples of the best-fitting spectra at different epochs in the left panels of Figure 5.

The uncertainties were estimated by Monte Carlo Markov Chain using the `chain` command in XSPEC. For each fit, we conservatively used 6 times the number of free parameters as walkers (e.g., 60 walkers if the model has 10 free parameters) and ran 50,000 steps per walker. The table of best-fitting parameters can be found on GitHub.[18] The correlation of $N_{\mathrm{H}}^{\mathrm{zxipcf}}$ and $\log\xi$ with respect to flux, time, and phase is shown in Figures 6 and B1. The derived absorption parameters exhibit considerable scatter, with $\log\xi \sim$ 1–3 erg cm s^{-1} and $N_{\mathrm{H}}^{\mathrm{zxipcf}} \sim (1\text{–}30) \times 10^{22}$ cm^{-2}. To investigate possible correlations between $N_{\mathrm{H}}^{\mathrm{zxipcf}}$, $\log\xi$, and the flux, time, and phase, we computed the Spearman rank correlation coefficient (r_s) using the `spearmanr` function in the `SciPy` package (P. Virtanen et al. 2020). To account for parameter uncertainties, we performed 50,000 Monte Carlo simulations by sampling each parameter within its measurement errors. The median $|r_s|$ values for all parameter pairs are below 0.3, and their 3σ lower bounds are below 0.1. We also examined the correlation between flux and individual phase intervals (e.g., 0.35–0.45, 0.45–0.60, and 0.60–0.75), finding median $|r_s|$ values below 0.45 with similarly 3σ lower bounds (<0.1). The associated median p-values are all greater than 0.05, indicating no statistically significant monotonic correlations.

Given the definition of the ionization parameter (C. B. Tarter et al. 1969)

$$\xi = \frac{L_{\mathrm{X}}}{n_{\mathrm{H}} R^2} = \frac{L_{\mathrm{X}}}{N_{\mathrm{H}} R} \cdot \frac{\Delta R}{R}, \tag{3}$$

where n_{H}, R, and ΔR represent the number density, the distance of the absorber from the X-ray source, and its thickness, respectively. The lack of correlation in $N_{\mathrm{H}}^{\mathrm{zxipcf}}$ and $\log\xi$ as L_{X} decreases by 1 order of magnitude suggests that either ΔR increases, R decreases, or both. However, the periodicity of the absorber implies a constant R, leaving an increase in ΔR as the only viable explanation.

---

[18] https://github.com/zlin-astr/Data_IGRJ17091_2025

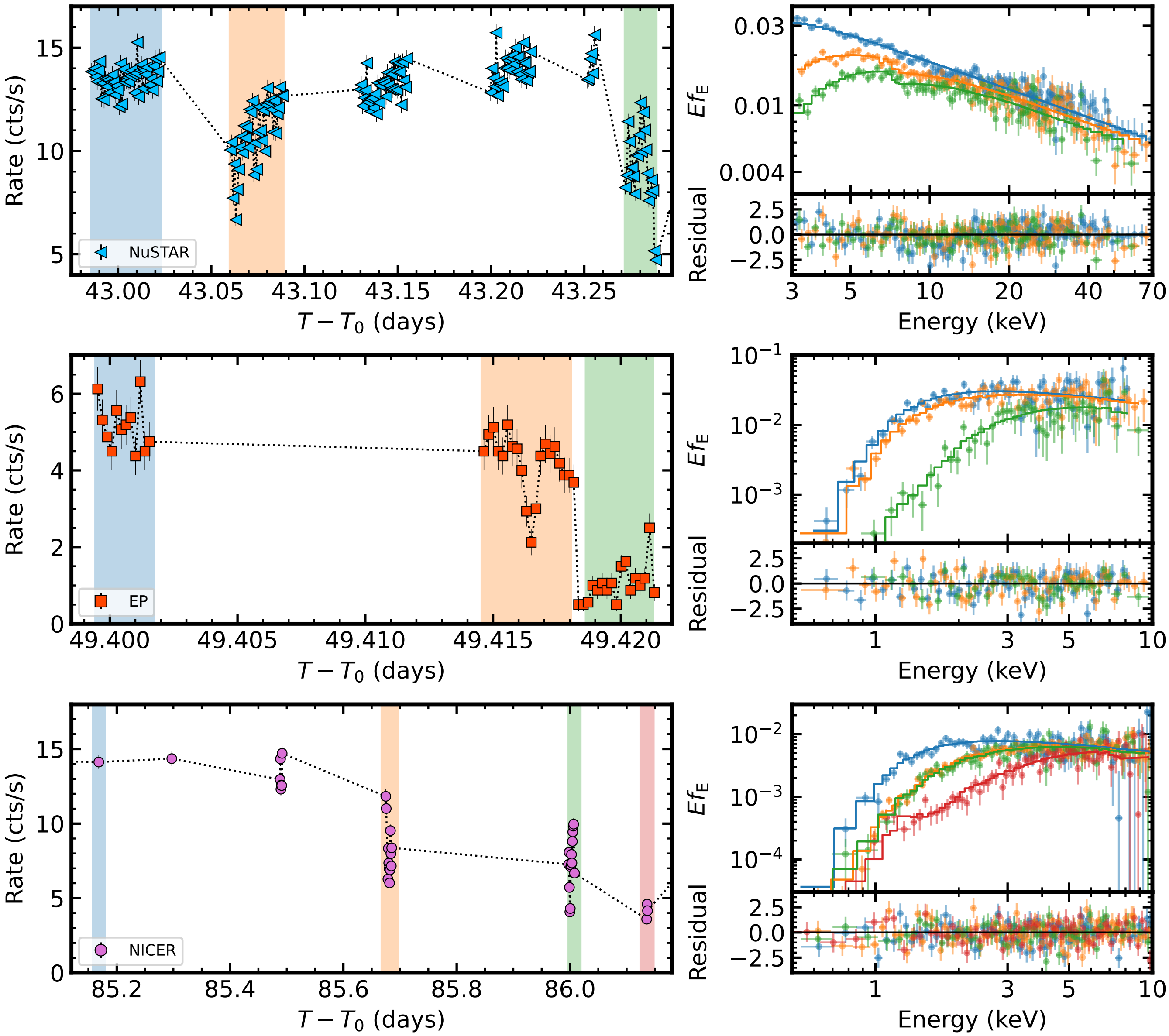

Figure 5. Three representative examples of light curve segments (left panels) used for joint spectral fitting, along with their corresponding best-fit spectra (right panels). The color of each spectrum corresponds to one GTI, including the shaded regions of the same color in the light curves. The blue region indicates the persistent interval, while the other shaded regions indicate the dipping intervals. We note here that we only show several example spectra for clarity; the data outside the shaded regions are also included in the joint fitting.

Furthermore, we detected a prominent absorption line centered around 7.2 keV during certain nondipping intervals, which is likely associated with highly ionized disk winds rather than the absorber responsible for the dipping episodes. This feature is discussed in detail in Appendix C.

3.3. Multiwavelength Analysis

3.3.1. Optical Counterpart

The optical light curve of IGR J17091–3624 is shown in the bottom panel of Figure 1. To explore possible correlations between X-ray and optical variability, we converted the optical magnitudes to fluxes and detrended the long-term decay using an exponential model. We then applied the same LSP analysis to the detrended optical light curves, as shown in the top panels of Figure A2. A spike is seen at 2.84 days with moderate significance ($>2\sigma$). This weaker detection in the optical data may result from limited coverage and/or X-ray reprocessing in the absorber.

Additionally, we computed the discrete cross-correlation function (CCF; M. Sun et al. 2018) between each detrended optical light curve and the detrended NICER light curve (on a GTI basis). No significant correlation or anticorrelation was found within a lag range of ±10 days, as shown in the bottom panels of Figure A2.

3.3.2. Radio Counterpart

We calculated the in-band photon index ($F \propto \nu^{\alpha}$) using the three ATCA observations and obtained α evolving from -0.16 ± 0.02 to -0.67 ± 0.04 within six days (see Table 1). These results suggest that the radio source exhibits an optically thin spectrum (R. P. Fender et al. 2004; R. Fender 2006), with the peak frequency progressively shifting to lower values as the luminosity decreases.

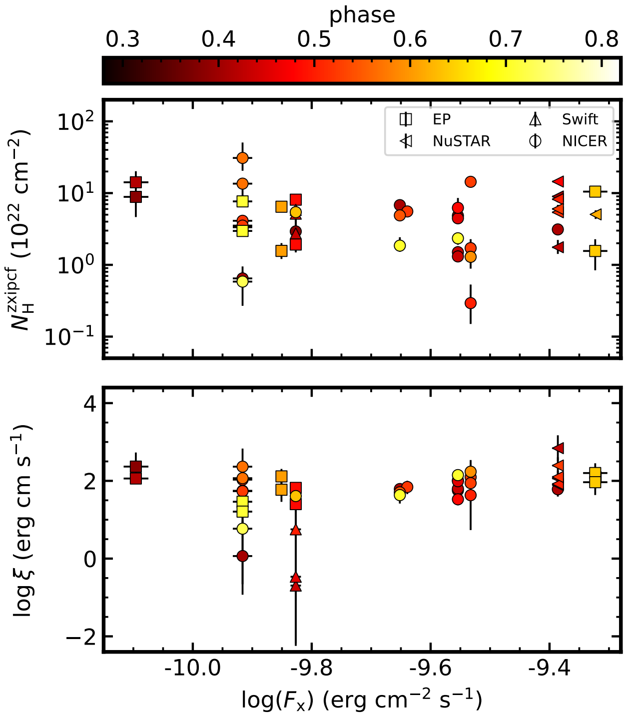

Figure 6. Relationship between the absorption parameters and the unabsorbed flux (0.5–10 keV). The color bar denotes the phase range associated with each data point. Top panel: $N_H^{\rm zxipcf}$ vs. $\log(F_x)$. Bottom panel: $\log \xi$ vs. $\log(F_x)$.

4. Discussion

In this work, we investigate the multiwavelength emission of IGR J17091–3624 during its hard-state-only outburst in 2025. For the first time, we identify quasiperiodic X-ray dipping behavior in the system, with a period of 2.83 ± 0.07 days and individual dips lasting approximately one day. Our X-ray spectral analysis shows that these dips are primarily caused by absorption and scattering from weakly ionized material along the line of sight. Neither the equivalent hydrogen column density nor the ionization parameter of the absorber shows any significant correlation with time, orbital phase, or luminosity. The optical light curves show a tentative signal at the same period as the X-ray dips, albeit with a significance just above 2σ. Meanwhile, our radio observations, limited to the early phase of the outburst, reveal a transition from a flat to a steep radio spectrum. In this section, we discuss the possible physical origins of these dips in the broader context of LMXBs and explore their implications for the physical properties of IGR J17091–3624.

4.1. Possible Origins of the Quasiperiodic Dips

In Section 3.1, we showed that the periodic dips likely developed gradually during the decay phase of the 2025 outburst. Notably, IGR J17091–3624 also exhibited dips during its 2011 outburst (M. Pahari et al. 2013), characterized by durations of ∼16 s and recurrence times of ∼120 s. These timescales are significantly shorter than those of the dips analyzed in this work, suggesting a different physical origin. We examined archival light curves from NICER, NuSTAR, Swift, and Rossi X-ray Timing Explorer/Proportional Counter Array, but found no evidence of prominent dips similar to those observed during the 2025 outburst.

Periodic X-ray dips in XRBs have been extensively studied and can arise from a variety of physical mechanisms. These include absorption by asymmetric structures of the accretion disk or associated accretion streams (e.g., N. E. White & J. H. Swank 1982; J. Frank et al. 1987; M. Díaz Trigo et al. 2006; D. R. Pasham & T. E. Strohmayer 2013; G. Raman et al. 2018; D. J. K. Buisson et al. 2021; A. Jana et al. 2022), shallow eclipses by the donor star (e.g., C. Hellier & K. O. Mason 1989; P. C. Schmidtke et al. 1993; K. Mukai et al. 2003), precession of tilted or warped disks (e.g., R. A. M. J. Wijers & J. E. Pringle 1999; G. I. Ogilvie & G. Dubus 2001; G. I. Ogilvie 2002; M. M. Kotze & P. A. Charles 2012; A. W. Shaw et al. 2013; R. G. Martin 2023), and obscuration by circumbinary material (e.g., P. Artymowicz & S. H. Lubow 1994, 1996; J.-M. Shi et al. 2012; D. J. D'Orazio et al. 2013).

In the scenario where obscuration arises from asymmetric structures in the outer accretion disk (N. E. White & J. H. Swank 1982; J. Frank et al. 1987), LMXBs undergo Roche-lobe-overflow transfer mass from the donor star via a stream that impacts the outer edge of the accretion disk. This interaction creates a dense, vertically extended, and azimuthally asymmetric structure, commonly referred to as the "bulge," at the stream–disk impact site. As the binary system orbits, this nonaxisymmetric bulge periodically crosses the observer's line of sight, giving rise to quasiperiodic dips in the X-ray light curve that reflect the orbital period of the system.

A detailed study of six LMXBs with periodic dips by M. Díaz Trigo et al. (2006) showed that the ionization parameter of the absorbing material typically lies in the range $\log \xi = 2$–4 erg cm s^{-1}. The absorber properties observed in IGR J17091–3624 during the dipping episodes are consistent with these findings. In this scenario, variations in the mass accretion rate, mass transfer rate, or the ionization state of the bulge can all influence the formation and geometry of the disk bulge (P. J. Armitage & M. Livio 1996, 1998), leading to structural differences between outbursts. Consequently, the sudden appearance of dips in IGR J17091–3624 during its 2025 outburst remains an open question.

While the disk bulge scenario provides a plausible explanation for the observations, we briefly consider alternative scenarios and explain why they are less likely in the case of IGR J17091–3624:

Partial obscuration by the donor star can also produce periodic dips in X-ray light curves. Since the dips observed in IGR J17091–3624 span approximately 0.36 in phase, this implies an eclipse fraction of $\Delta_{\rm ecl} = 0.36$. We can then estimate the donor star radius ($R_{\rm d}$) relative to its Roche-lobe radius ($R_{\rm L,d}$) using the following relations (G. A. Chanan et al. 1976; P. P. Eggleton 1983; D. Porquet et al. 2005):

$$\sin i \cos(\pi \Delta_{\rm ecl}) = \left[1 - (R_{\rm d}/a)^2\right]^{1/2}$$
$$\frac{R_{\rm L,d}}{a} = \frac{0.49 q^{2/3}}{0.6 q^{2/3} + \ln(1 + q^{1/3})}, \qquad (4)$$

where i is the inclination angle, a is the binary separation, and $q = M_{\rm d}/M_{\rm c}$ is the mass ratio between the donor star mass ($M_{\rm d}$) and the compact object mass ($M_{\rm c}$). For $\Delta_{\rm ecl} = 0.36$, the derived $R_{\rm d}$ would exceed $1.5 R_{\rm L,d}$, resulting in an unphysical configuration. Moreover, such dips would be expected to occur more persistently and should not have been missed in the early

NICER observations in 2025. We therefore do not favor this scenario.

Alternative scenarios, such as the precession of a tilted or warped accretion disk under the tidal forces from the donor star (G. I. Ogilvie & G. Dubus 2001; G. I. Ogilvie 2002), could in principle produce periodic modulations in optical and X-ray light curves. Such precession could occur over timescales of a few to several hundred days (see, e.g., M. I. Kudryavtsev et al. 1989; L. Homer et al. 2001; M. M. Kotze & P. A. Charles 2012), often leading to gradual, sinusoidal variations in X-ray luminosity (e.g., M. M. Kotze & P. A. Charles 2012; A. W. Shaw et al. 2013). In the case of IGR J17091–3624, as shown by the X-ray light curve, the dips are sharp, intermittent, and exhibit varying profiles. Outside of the dipping intervals, the light curve remains relatively flat. Thus, the observed 2.84 day period is unlikely to be associated with disk precession.

Circumbinary disks, which typically reside at large distances from the central binary (R. M. Lau et al. 2019; D. Lai & D. J. Muñoz 2023), could in principle partially obscure the inner emission and produce absorption features in the light curves. To explain the appearance of dips in IGR J17091–3624 exclusively during the 2025 outburst, one would need to invoke a scenario in which a circumbinary disk gradually moved into the observer's line of sight, for example, through precession. However, such a scenario would likely lead to a gradual increase in the phase duration of the dips over time. This expected behavior is inconsistent with our observations, as the dipping interval with a phase duration of 0.36 was already established shortly after the dipping feature emerged. Therefore, we do not favor this scenario either.

4.2. Physical Implication of the Periodic Dips

In the following, we further explore the implications of the observed dips under the assumption that the dip period corresponds to the binary orbital period.

First, the presence of absorption dips implies a relatively high inclination angle, as the observer's line of sight must intersect vertically extended structures at the outer edge of the accretion disk. According to J. Frank et al. (1987), XRBs that exhibit dipping behavior typically have orbital inclinations between 60° and 75°. At sufficiently high inclinations, eclipses may occur, whereas at lower inclinations, the observer's line of sight typically does not intersect the outer disk rim, and dips are less likely to be detected. However, reflection modeling estimates the inclination of IGR J17091–3624 at 20°–45° (Y. Xu et al. 2017; Y. Wang et al. 2018; J. Wang et al. 2024); all these studies favor a value considerably lower than the inclination suggested by the dipping behavior. Similar discrepancies between inclinations derived from reflection modeling and those obtained from dynamical measurements have been reported in other XRBs, such as XTE J1550–564 (R. M. T. Connors et al. 2019). These differences may be explained by a warped accretion disk, potentially caused by a misalignment between the black hole spin axis and the binary orbital axis (e.g., J. M. Bardeen & J. A. Petterson 1975; P. Natarajan & J. E. Pringle 1998; M. Liska et al. 2018, 2021).

Based on the optical brightness of IGR J17091–3624 detected during its quiescent state ($r' \sim 20.8$ and $i' \sim 19.5$; K. Fialova et al. 2025), and adopting a distance of < 25 kpc (D. Altamirano et al. 2011), the donor star's mass is estimated to be less than approximately $10\,M_{\odot}$. Otherwise, the blackbody emission in the r' and i' bands would be brighter than that observed in the quiescent state. Adopting a typical compact object mass of $M_{\rm c} = 1$–$15\,M_{\odot}$ and a donor mass of $M_{\rm d} = 0.1$–$10\,M_{\odot}$, we estimate the binary separation to be $a = 10$–$30\,R_{\odot}$ for an orbital period of $P_{\rm orb} = 2.84$ days, based on Kepler's third law:

$$a = \left[\frac{G(M_c + M_d)P_{\rm orb}^2}{4\pi^2}\right]^{1/3}. \quad (5)$$

Using equation Equation (4), the Roche-lobe radius is determined to be $R_{\rm L,d} = 2$–$10\,R_{\odot}$. Assuming stable mass transfer occurs when the donor star fills its Roche lobe (i.e., $R_{\rm d} = R_{\rm L,d}$), the corresponding donor radius across the considered mass range ($M_{\rm d} = 0.1$–$10\,M_{\odot}$) exceeds the empirical radii expected for main-sequence stars (Z. Eker et al. 2018). This suggests that the donor has likely evolved into a giant star. Moreover, giant stars typically have radii exceeding $10\,R_{\odot}$, which would overfill the estimated Roche lobe in this system. This suggests that the donor in IGR J17091–3624 is likely a (partially) stripped giant, an evolved star that has lost part of its envelope, similar to the donors observed in V404 Cyg (A. R. King 1993) and XTE J1550–564 (J. A. Orosz et al. 2011b).

We also independently verified this possibility by evolving a `MESA` model (B. Paxton et al. 2011, 2013, 2015, 2018, 2019; A. S. Jermyn et al. 2023) of a $1.2\,M_{\odot}$ main-sequence donor in a binary with a $10\,M_{\odot}$ black hole (treated as a point mass) and an initial orbital period of ∼2.8 days. The system does not initiate stable mass transfer until the donor radius expands to $\sim 4\,R_{\odot}$, which occurs well beyond core hydrogen exhaustion ($\sim 1.8\,R_{\odot}$ for solar metallicity). This supports the conclusion that the donor in IGR J17091–3624 has likely evolved into a giant star. Further optical and infrared observations during the quiescent state would help confirm this interpretation. For instance, orbital modulation in the optical/infrared light curves, caused by the asymmetric geometry of the Roche-lobe-filling donor, should exhibit the same period as the X-ray dips (e.g., J. A. Orosz et al. 2007, 2011a). Additionally, infrared spectroscopy could help constrain the spectral type of the donor star (e.g., J. Casares & P. A. Charles 1994; J. Greiner et al. 2001).

Acknowledgments

We thank the anonymous referee for the constructive comments, which have helped improve the manuscript. We thank Ileyk El Mellah for the useful discussion. This research was supported by the National Natural Science Foundation of China (NSFC) under grant No. 12588202; by the New Cornerstone Science Foundation through the New Cornerstone Investigator Program and the XPLORER PRIZE; by the Strategic Priority Program of the Chinese Academy of Sciences under grant No. XDB0550203, and by the China-Chile Joint Research Fund (CCJRF No.2301) and the Chinese Academy of Sciences South America Center for Astronomy (CASSACA) Key Research Project E52H540301. Z.G. is funded by ANID, Millennium Science Initiative, AIM23-001.

Appendix A
Detailed Information on Optical Variability

Based on the SOAR imaging data, IGR J17091–3624 can be partially resolved from a nearby contaminating source. To robustly determine whether the observed optical variability originates from our target, we performed image subtraction using the `HOTPANTS` package (A. Becker 2015), which implements the algorithm developed by C. Alard & R. H. Lupton (1998). The resulting difference image (see Figure A1) clearly shows that the variability arises from IGR J17091–3624, while the nearby source remains relatively stable.

In this section, we present the LSPs of the detrended optical light curves, together with the CCFs between each detrended optical light curve and the detrended NICER light curve, in Figure A2.

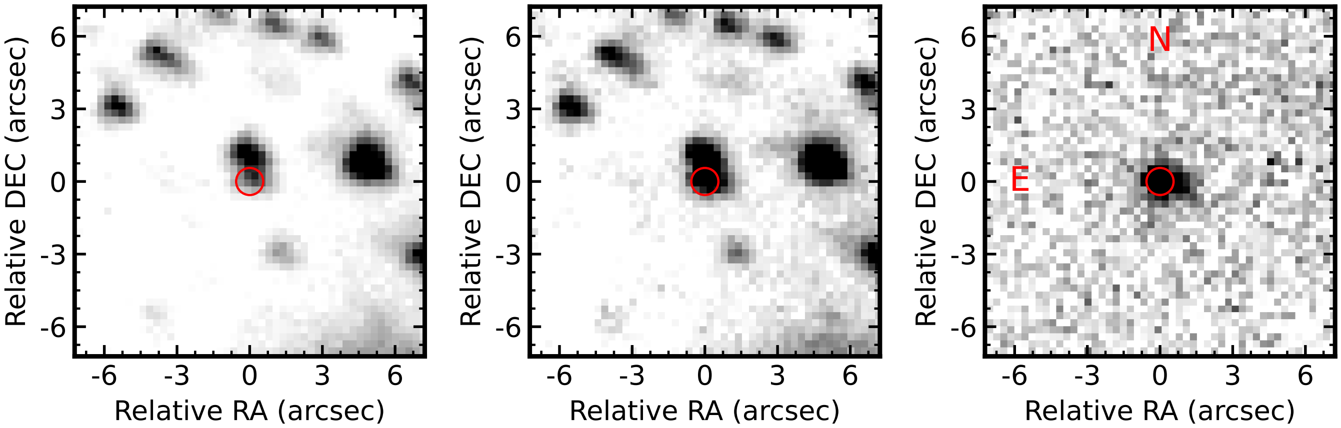

Figure A1. Left panel: SOAR image taken at 125 days. Middle panel: SOAR image taken at 85 days. Right panel: difference image between 85 and 125 days. Images were observed in the i' band. The red circle, marking the position of IGR J17091–3624, is centered at R.A. = $257\overset{\circ}{.}28166 \pm 0\overset{''}{.}26$ and decl. = $-36\overset{\circ}{.}40711 \pm 0\overset{''}{.}14$ (J2000), as determined from the ATCA measurements.

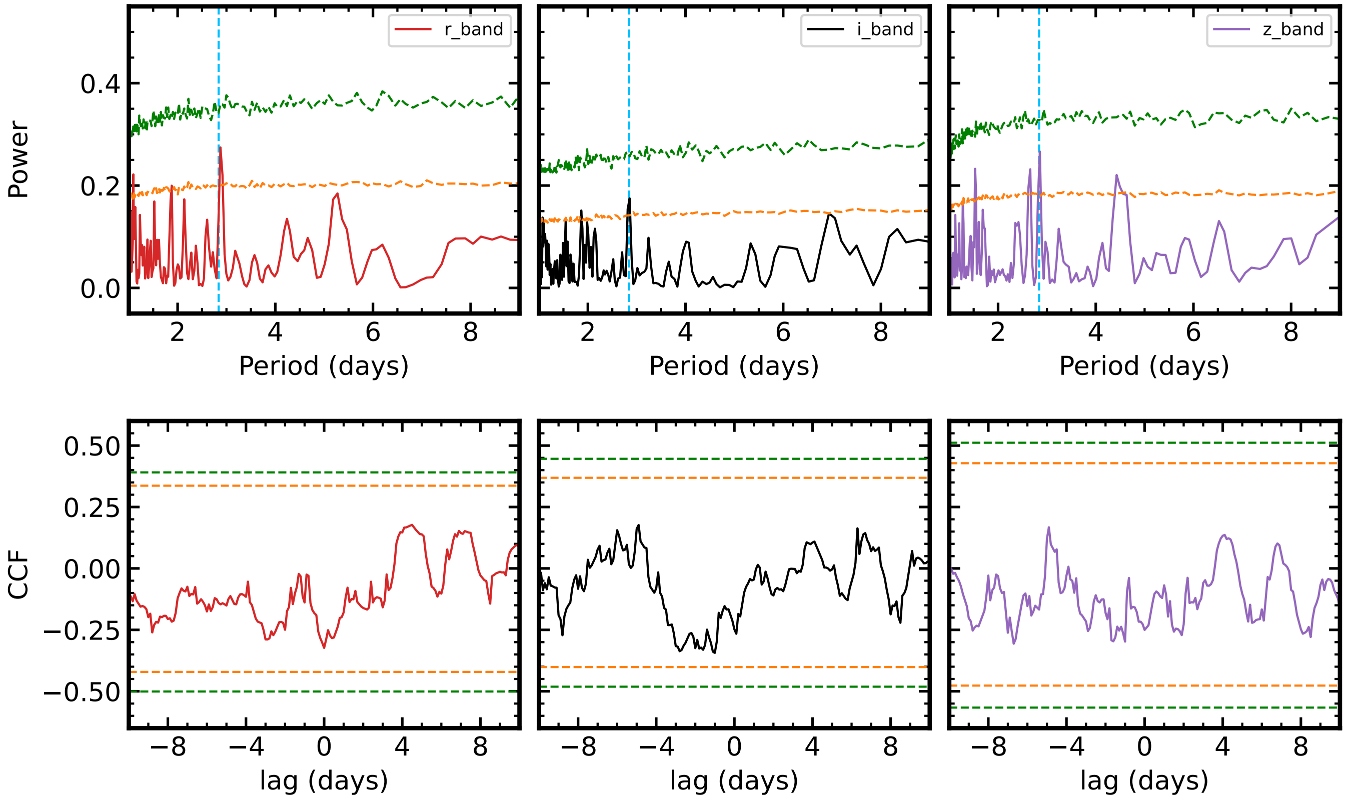

Figure A2. Top panels: LSP of the detrended optical light curve in the r' (left), i' (middle), and z' (right) filters. Bottom panels: CCF between the detrended NICER and optical light curves. The orange and green dashed lines indicate the 95% (2σ) and 99.73% (3σ) significance level, respectively. The vertical blue dashed line marks the period of 2.84 days.

Appendix B
Parameters of the Absorption Dips

In this section, we present the evolution of the absorption parameters in phase and time space, as shown in Figure B1.

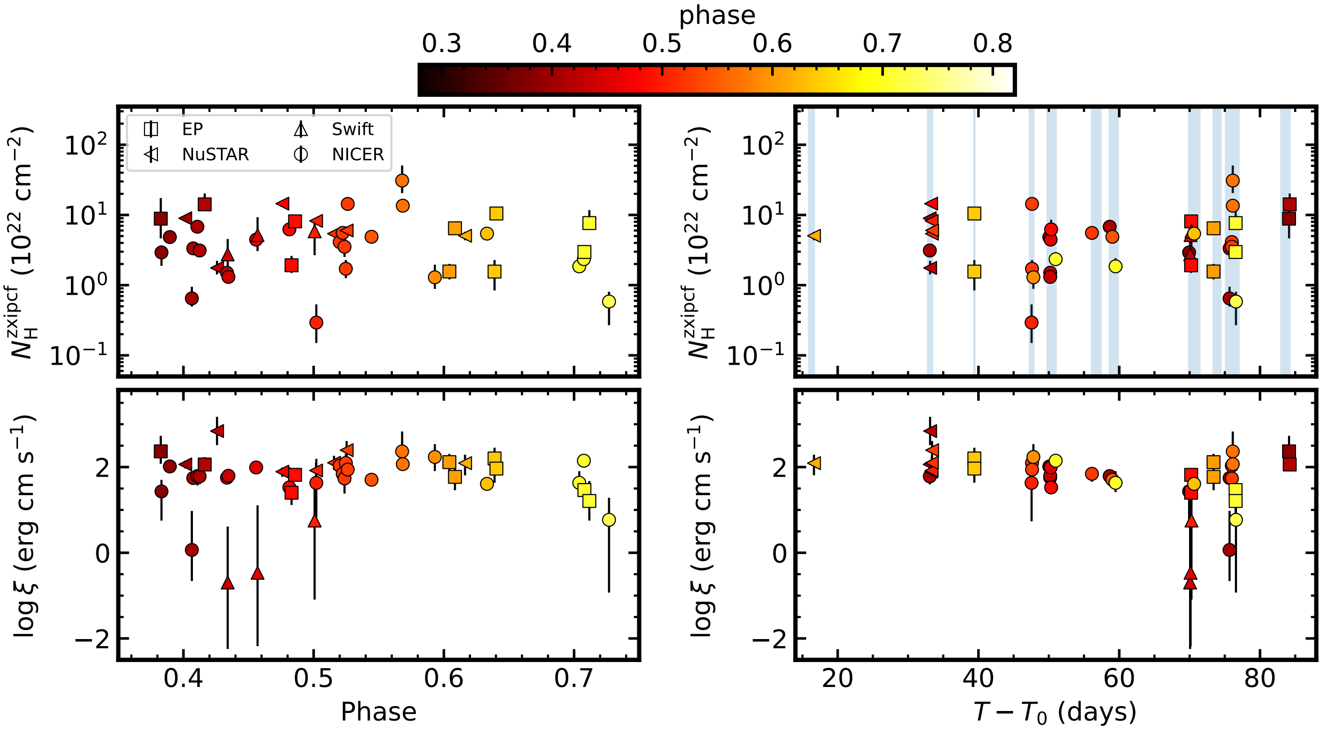

Figure B1. left panels: best-fitting absorption parameters shown in the phase space. The color bar represents the phase range corresponding to each data point. Right panels: best-fitting absorption parameters shown in the time space. The blue shaded region indicates the time coverage for the joint fit episodes.

Appendix C
Potential Disk Wind during the Hard State

In several individual X-ray spectra of IGR J17091–3624, an absorption feature around 7 keV occasionally appears. The observation by EP at 81.3 days shows the most prominent example (see Figure C1). We convolve a `gabs` component with the continuum, which significantly improves the fit statistics by ΔC-stat = 19 for three additional dof. The best-fitting centroid energy is $7.2^{+0.3}_{-0.2}$ keV, consistent with the energy range of Fe K edge or blueshifted Fe Kα lines (e.g., F. Fürst et al. 2011; K. I. I. Koljonen & J. A. Tomsick 2020). Since the observation was made during the nondipping episodes, this feature likely has a different origin from the other absorption components observed and possibly associated with disk winds, as seen in previous outbursts in both the hard (e.g., Y. Wang et al. 2018) and soft states (e.g., J. Wang et al. 2024). Hydrodynamic simulations suggest that, during the hard state of XRBs, disk winds may be launched with higher velocities and degrees of ionization compared to those observed in the soft state (N. Higginbottom et al. 2020). A detailed analysis of the absorption lines will be provided in a separate work.

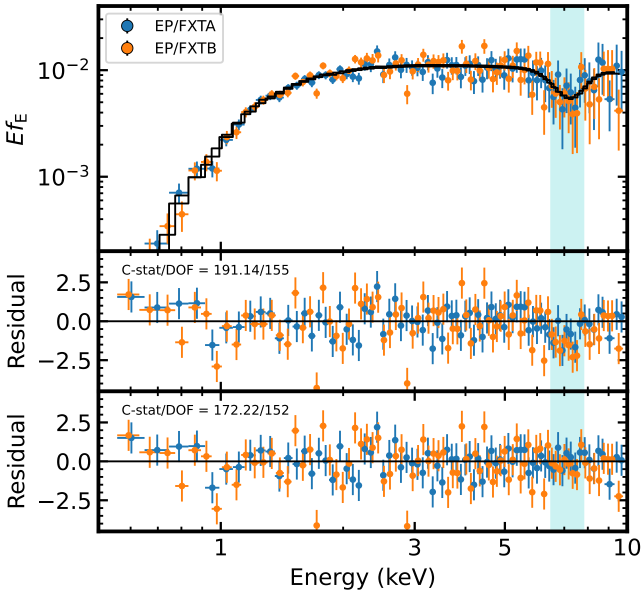

Figure C1. EP spectrum observed at 81.3 days (nondipping episode). The cyan shaded region highlights a prominent absorption feature centered at 7.2 keV. The bottom two panels show the residuals of the fit without and with an additional `gabs` component in the continuum model (`constant×tbabs×powerlaw`). The fit statistics (C-stat/dof) for both models are shown in the upper left corner.

ORCID iDs

Zikun Lin https://orcid.org/0000-0001-9576-1870
Yanan Wang https://orcid.org/0000-0003-3207-5237
Shuyuan Wei https://orcid.org/0009-0005-5669-8465
Yongkang Sun https://orcid.org/0000-0002-3935-2666
Long Ji https://orcid.org/0000-0001-9599-7285
Samaporn Tinyanont https://orcid.org/0000-0002-1481-4676
Meng Sun https://orcid.org/0000-0001-9037-6180
Song Wang https://orcid.org/0000-0003-3116-5038
Diego Altamirano https://orcid.org/0000-0002-3422-0074
Douglas J. K. Buisson https://orcid.org/0000-0002-5341-6929
Wenxiong Li https://orcid.org/0000-0002-0096-3523
Qian Chen https://orcid.org/0009-0003-4854-3610
Jifeng Liu https://orcid.org/0000-0002-2874-2706
Shuang-Nan Zhang https://orcid.org/0000-0001-5586-1017
Wei Wang https://orcid.org/0000-0002-9702-4441
Zhen Guo https://orcid.org/0000-0003-0292-4832
Pathompong Butpan https://orcid.org/0000-0003-1012-8086
Rungrit Anutarawiramkul https://orcid.org/0009-0006-9630-5352

References

Adegoke, O. K., Garcia, J. A., Mastroserio, G., et al. 2025, ApJ, 995, 143
Alard, C., & Lupton, R. H. 1998, ApJ, 503, 325
Altamirano, D., Belloni, T., Linares, M., et al. 2011, ApJL, 742, L17
Armitage, P. J., & Livio, M. 1996, ApJ, 470, 1024
Armitage, P. J., & Livio, M. 1998, ApJ, 493, 898
Arnaud, K. A. 1996, ASPC, 101, 17
Artymowicz, P., & Lubow, S. H. 1994, ApJ, 421, 651
Artymowicz, P., & Lubow, S. H. 1996, ApJL, 467, L77
Astropy Collaboration, Price-Whelan, A. M., Lim, P. L., et al. 2022, ApJ, 935, 167
Avakyan, A., Neumann, M., Zainab, A., et al. 2023, A&A, 675, A199
Bardeen, J. M., & Petterson, J. A. 1975, ApJL, 195, L65
Becker, A., 2015 High Order Transform of PSF ANd Template Subtraction, Astrophysics Source Code Library, ascl:1504.004
Blackburn, J. K. 1995, ASPC, 77, 367
Boirin, L., Méndez, M., Díaz Trigo, M., Parmar, A. N., & Kaastra, J. S. 2005, A&A, 436, 195
Buisson, D. J. K., Altamirano, D., Armas Padilla, M., et al. 2021, MNRAS, 503, 5600
Burrows, D. N., Hill, J. E., Nousek, J. A., et al. 2005, SSRv, 120, 165
Capitanio, F., Giroletti, M., Molina, M., et al. 2009, ApJ, 690, 1621
CASA Team, Bean, B., Bhatnagar, S., et al. 2022, PASP, 134, 114501
Casares, J., & Charles, P. A. 1994, MNRAS, 271, L5
Cash, W. 1979, ApJ, 228, 939
Chanan, G. A., Middleditch, J., & Nelson, J. E. 1976, ApJ, 208, 512
Connolly, S. D., 2016 DELightcurveSimulation: Light Curve Simulation code, Astrophysics Source Code Library, ascl:1602.012
Connors, R. M. T., García, J. A., Steiner, J. F., et al. 2019, ApJ, 882, 179
Corral-Santana, J. M., Torres, M. A. P., Shahbaz, T., et al. 2018, MNRAS, 475, 1036
Court, J. M. C., Altamirano, D., Pereyra, M., et al. 2017, MNRAS, 468, 4748
Crampton, D., Cowley, A. P., Stauffer, J., Ianna, P., & Hutchings, J. B. 1986, ApJ, 306, 599
Debnath, D., Srimani, S., & Chang, H.-K. 2025, ApJ, 989, 165
Díaz Trigo, M., Parmar, A. N., Boirin, L., Méndez, M., & Kaastra, J. S. 2006, A&A, 445, 179
Díaz Trigo, M., Parmar, A. N., Boirin, L., et al. 2009, A&A, 493, 145
Díaz Trigo, M., Sidoli, L., Boirin, L., & Parmar, A. N. 2012, A&A, 543, A50
D'Orazio, D. J., Haiman, Z., & MacFadyen, A. 2013, MNRAS, 436, 2997
Eggleton, P. P. 1983, ApJ, 268, 368
Eker, Z., Bakış,, V., Bilir, S., et al. 2018, MNRAS, 479, 5491
Emmanoulopoulos, D., McHardy, I. M., & Papadakis, I. E. 2013, MNRAS, 433, 907
Evans, P. A., Beardmore, A. P., Page, K. L., et al. 2007, A&A, 469, 379
Evans, P. A., Beardmore, A. P., Page, K. L., et al. 2009, MNRAS, 397, 1177
Ewing, M., Parra, M., Mastroserio, G., et al. 2025, MNRAS, 541, 1774
Fender, R. 2006, in Compact Stellar X-ray Sources, ed. W. H. G. Lewin & M. van der Klis, 39 (Cambridge Univ. Press), 381
Fender, R. P., Belloni, T. M., & Gallo, E. 2004, MNRAS, 355, 1105
Fialova, K., Saikia, P., Russell, D. M., et al. 2025, ATel, 17065, 1
Frank, J., King, A. R., & Lasota, J. P. 1987, A&A, 178, 137
Fürst, F., Suchy, S., Kreykenbohm, I., et al. 2011, A&A, 535, A9
Gendreau, K. C., Arzoumanian, Z., Adkins, P. W., et al. 2016, SPIE, 9905, 99051H
Greiner, J., Cuby, J. G., McCaughrean, M. J., Castro-Tirado, A. J., & Mennickent, R. E. 2001, A&A, 373, L37
Harrison, F. A., Craig, W. W., Christensen, F. E., et al. 2013, ApJ, 770, 103
HEASARC, 2014 HEAsoft: Unified Release of FTOOLS and XANADU, Astrophysics Source Code Library, ascl:1408.004
Hellier, C., & Mason, K. O. 1989, MNRAS, 239, 715
Higginbottom, N., Knigge, C., Sim, S. A., et al. 2020, MNRAS, 492, 5271
Homer, L., Charles, P. A., Hakala, P., et al. 2001, MNRAS, 322, 827
Huppenkothen, D., Bachetti, M., Stevens, A. L., et al. 2019, ApJ, 881, 39
Jana, A., Naik, S., Jaisawal, G. K., et al. 2022, MNRAS, 511, 3922
Jermyn, A. S., Bauer, E. B., Schwab, J., et al. 2023, ApJS, 265, 15
Kaastra, J. S. 2017, A&A, 605, A51
Kaastra, J. S., & Bleeker, J. A. M. 2016, A&A, 587, A151
Kajava, J. J. E., Motta, S. E., Sanna, A., et al. 2019, MNRAS, 488, L18
King, A. R. 1993, MNRAS, 260, L5
King, A. R., & Ritter, H. 1998, MNRAS, 293, L42
Koljonen, K. I. I., & Tomsick, J. A. 2020, A&A, 639, A13
Kotze, M. M., & Charles, P. A. 2012, MNRAS, 420, 1575
Krimm, H. A., Barthelmy, S. D., Baumgartner, W., et al. 2011, ATel, 3144, 1
Kudryavtsev, M. I., Mamontova, N. A., Svertilov, S. I., & Tolstaya, E. D. 1989, SvAL, 15, 466
Kuulkers, E., Kouveliotou, C., Belloni, T., et al. 2013, A&A, 552, A32
Kuulkers, E., Lutovinov, A., Parmar, A., et al. 2003, ATel, 149, 1
Lai, D., & Muñoz, D. J. 2023, ARA&A, 61, 517
Lau, R. M., Heida, M., Walton, D. J., et al. 2019, ApJ, 878, 71
Liska, M., Hesp, C., Tchekhovskoy, A., et al. 2018, MNRAS, 474, L81
Liska, M., Hesp, C., Tchekhovskoy, A., et al. 2021, MNRAS, 507, 983
Martin, R. G. 2023, MNRAS, 523, L75
Miller, J. M., Draghis, P., Gendreau, K., & Arzoumanian, Z. 2022, ATel, 15282, 1
Miller, J. M., Reynolds, M., Kennea, J., King, A. L., & Tomsick, J. 2016, ATel, 8742, 1
Mitsuda, K., Inoue, H., Koyama, K., et al. 1984, PASJ, 36, 741

Mukai, K., Still, M., & Ringwald, F. A. 2003, ApJ, 594, 428
Natarajan, P., & Pringle, J. E. 1998, ApJL, 506, L97
Ogilvie, G. I. 2002, MNRAS, 330, 937
Ogilvie, G. I., & Dubus, G. 2001, MNRAS, 320, 485
Onken, C. A., Wolf, C., Bessell, M. S., et al. 2024, PASA, 41, e061
Orosz, J. A., McClintock, J. E., Aufdenberg, J. P., et al. 2011a, ApJ, 742, 84
Orosz, J. A., McClintock, J. E., Narayan, R., et al. 2007, Natur, 449, 872
Orosz, J. A., Steiner, J. F., McClintock, J. E., et al. 2011b, ApJ, 730, 75
Pahari, M., Yadav, J. S., Rodriguez, J., et al. 2013, ApJ, 778, 46
Pasham, D. R., & Strohmayer, T. E. 2013, ApJ, 764, 93
Paxton, B., Bildsten, L., Dotter, A., et al. 2011, ApJS, 192, 3
Paxton, B., Cantiello, M., Arras, P., et al. 2013, ApJS, 208, 4
Paxton, B., Marchant, P., Schwab, J., et al. 2015, ApJS, 220, 15
Paxton, B., Schwab, J., Bauer, E. B., et al. 2018, ApJS, 234, 34
Paxton, B., Smolec, R., Schwab, J., et al. 2019, ApJS, 243, 10
Porquet, D., Grosso, N., Bélanger, G., et al. 2005, A&A, 443, 571
Raman, G., Maitra, C., & Paul, B. 2018, MNRAS, 477, 5358
Rodriguez, J., Ferrigno, C., Bouchet, T., et al. 2025, ATel, 17034, 1
Saikia, P., Russell, D. M., Rout, S., et al. 2025, ATel, 17166, 1
Schmidtke, P. C., McGrath, T. K., Cowley, A. P., & Frattare, L. M. 1993, PASP, 105, 863
Shahbaz, T., Charles, P. A., & King, A. R. 1998, MNRAS, 301, 382
Shaw, A. W., Charles, P. A., Bird, A. J., et al. 2013, MNRAS, 433, 740
Shi, J.-M., Krolik, J. H., Lubow, S. H., & Hawley, J. F. 2012, ApJ, 749, 118
Shidatsu, M., Ueda, Y., Nakahira, S., et al. 2013, ApJ, 779, 26
Stelzer, B., Wilms, J., Staubert, R., Gruber, D., & Rothschild, R. 1999, A&A, 342, 736
Sun, M., Grier, C. J., & Peterson, B. M., 2018 PyCCF: Python Cross Correlation Function for Reverberation Mapping Studies, Astrophysics Source Code Library, ascl:1805.032
Tarter, C. B., Tucker, W. H., & Salpeter, E. E. 1969, ApJ, 156, 943
Verner, D. A., Ferland, G. J., Korista, K. T., & Yakovlev, D. G. 1996, ApJ, 465, 487
Vincentelli, F., Woahene-Demehin, S., Jaisawal, G. K., et al. 2025, ATel, 17038, 1
Virtanen, P., Gommers, R., Oliphant, T. E., et al. 2020, NatMe, 17, 261
Wang, J., Kara, E., García, J. A., et al. 2024, ApJ, 963, 14
Wang, Y., Méndez, M., Altamirano, D., et al. 2018, MNRAS, 478, 4837
Weisskopf, M. C., Soffitta, P., Baldini, L., et al. 2022, JATIS, 8, 026002
White, N. E., & Swank, J. H. 1982, ApJL, 253, L61
Wijers, R. A. M. J., & Pringle, J. E. 1999, MNRAS, 308, 207
Wilms, J., Allen, A., & McCray, R. 2000, ApJ, 542, 914
Xu, Y., García, J. A., Fürst, F., et al. 2017, ApJ, 851, 103
Yuan, W., Zhang, C., Chen, Y., & Ling, Z. 2022, in Handbook of X-ray and Gamma-ray Astrophysics, ed. C. Bambi & A. Sangangelo (Springer), 86